Transient and steady state CO oxidation kinetics on nanolithographically prepared supported Pd model catalysts: Experiments and simulations

M. Laurin and V. Johánek
Fritz-Haber-Institut der Max-Planck-Gesselschaft, Faradayweg 4-6, D-14195 Berlin, Germany

A. W. Grant and B. Kasemo
Department of Applied Physics, Chalmers University of Technology, S-412 96 Göteborg, Sweden

J. Libuda[a] and H.-J. Freund
Fritz-Haber-Institut der Max-Planck-Gesselschaft, Faradayweg 4-6, D-14195 Berlin, Germany

(Received 10 March 2005; accepted 16 May 2005; published online 5 August 2005)

Applying molecular-beam methods to a nanolithographically prepared planar Pd/SiO_2 model catalyst, we have performed a detailed study of the kinetics of CO oxidation. The model catalyst was prepared by electron-beam lithography, allowing individual control of particle size and position. The sample was structurally characterized by atomic force microscopy and scanning electron microscopy before and after reaction. In the kinetic experiments, the O-rich and CO-rich regimes were investigated systematically with respect to their transient and steady-state behaviors, both under bistable and monostable reaction conditions. Separate molecular beams were used in order to supply the reactants, allowing individual control over the reactant fluxes. The desorbing CO_2 was detected by both angle-resolved and angle-integrated mass spectrometries. The experimental results were analyzed using different types of microkinetic models, including a detailed reaction-diffusion model, which takes into account the structural parameters of the catalyst as well as scattering of the reactants from the support. The model quantitatively reproduces the results as a function of the reactant fluxes and the surface temperature. Various kinetic effects observed are discussed in detail on the basis of the model. Specifically, it is shown that under conditions of limited oxygen mobility, the switching behavior between the kinetic regimes is largely driven by the surface mobility of CO. © *2005 American Institute of Physics*. [DOI: 10.1063/1.1949167]

I. INTRODUCTION

Many heterogeneous catalysts for industrial and environmental applications are based on nanometer-sized metal particles finely dispersed on oxide supports.[1] Experimentally, it is well established that reaction kinetics on such supported systems can differ strongly from the kinetics on single-crystal surfaces.[2–4] Understanding and controlling these effects remain the key challenges in catalyst development.

Numerous effects have been proposed, which can contribute to the different kinetics on nanometer-sized supported particles. Many of them assume modifications of the adsorption and reaction properties for small particles. However, there are also pure kinetic effects, which result from the limited size of the particles, i.e., not derived from changes of their electronic and adsorption properties. Examples of such "nanoscale" kinetic phenomena are the so-called communication effects resulting from the coupling of surface areas with different adsorption or reaction behavior via surface diffusion[5–7] or coverage fluctuations in confined surface regions.[8,9] Both effects are intimately related to the surface mobility of the reactants.

In spite of a large number of theoretical investigations and considerable theoretical understanding, there is very little experimental data available on such phenomena.[3,10–13] This lack derives from experimental challenges associated with such studies on real catalysts. First, the enormous complexity of the surfaces of real heterogeneous catalysts often precludes detailed insights into the kinetics at the molecular and single-particle level. Secondly, only a few experimental techniques can provide sufficiently detailed experimental data on surface kinetics and transport phenomena under reaction conditions, even if the samples are "ideal."

In order to overcome these problems, our group and others have recently started to apply molecular-beam techniques to model catalysts (see Refs. 2, 4, and 14–16, and references therein). Here, the use of model catalysts reduces the complexity of the surfaces to a controllable level, and the molecular-beam reactor provides a maximum level of control over the reaction conditions.

Recently, we have started to investigate reaction kinetics on a supported model catalyst prepared by electron-beam lithography (EBL).[9,17] This preparation method has been used only lately for reactivity studies in ultrahigh vacuum (UHV). It provides an exceptional level of control over structural parameters, including homogeneous particle sizes, exactly controllable particle distances and positions, and variable aspect ratios (see, e.g., Refs. 18 and 19).

Combining these well-defined planar model catalysts with molecular-beam techniques makes it possible to individually control the reactant fluxes to different surface re-

[a]Author to whom correspondence should be addressed. Fax: +49-30-84134139. Electronic mail: libuda@fhi-berlin.mpg.de

gions of the supported particles. On the one hand, such experiments allow us to simulate situations in which different parts of a particle are exposed to different reactant fluxes. On real catalysts such a situation may arise from coupling between nonequivalent surface areas via fast surface diffusion (see, e.g., Ref. 3). On the other hand, this type of experiment makes it possible to artificially generate coverage gradients on a single-particle surface and, as a result, facilitates measurements of the surface mobility of reactants under reaction conditions.[17,20,21]

In a recent study it was demonstrated that the global reaction kinetics and bistability behavior can be measured on such samples and that the kinetics is well described by a simple homogeneous surface model.[9] In addition, we have started to develop a detailed microkinetic description based on a reaction-diffusion (RD) model in order to obtain a quantitative description of the local distribution of reaction rates over the particle surface. (Local rates and coverages on a single, multifaceted particle has been described by Monte Carlo simulations,[22] but did not include asymmetric gas flux and communication with the support.) The RD model explicitly takes into account the morphology of the model catalysts surface, the geometry of the molecular-beam experiment as well as backscattering of reactants and products from the support.[21] In this work, we apply this model to simulate the corresponding experimental data and analyze the kinetic phenomena observed under the steady-state and transient conditions.

II. EXPERIMENTAL METHODS AND KINETIC MODELS

A. Model catalysts

The preparation of the Pd/SiO_2 model catalyst by EBL has been described in detail previously (Ref. 21, see also Ref. 18). In general, the advantage of the method is that it provides a high level of control over structural parameters such as particle size, shape, and position. Briefly, EBL is a serial technique in which an electron beam is rastered across the preselected areas of the surface of an electron sensitive polymeric resist, creating a computer-generated pattern in this film. In this work we used as a support for the nanoparticles, a 0.4-μm-thick thermal oxide layer grown on Si(100) substrate. The electron sensitive resist was first spun on the oxide layer, and then exposed to the electron beam at the preselected areas. After dissolving the electron-exposed polymer, a 500-nm-thick film of Pd (99.95% purity, K.A. Rasmussen, AB) was vapor deposited in an electron-beam deposition system (AVAC HVC-600). After lift-off (dissolution) of the resist, removing the unwanted Pd, the sample with the SiO_2-supported Pd particles was cleaned by an oxidation reduction cycle in a flow reactor using 5% O_2 in Ar (770 K) and 2% H_2 in Ar (820 K). Subsequently, the EBL sample fabricated at the MC2 Laboratory at Chalmers University of Technology (Göteborg, Sweden) was transported to the Fritz-Haber-Institute (Berlin, Germany), where the molecular-beam experiments were performed. In the molecular-beam ultrahigh vacuum (UHV) apparatus (see Sec. II B), the sample was further cleaned by oxidation reduction cycles in O_2 ($\sim 4\times10^{-4}$ mbar, 2 h, 650 K) and CO.

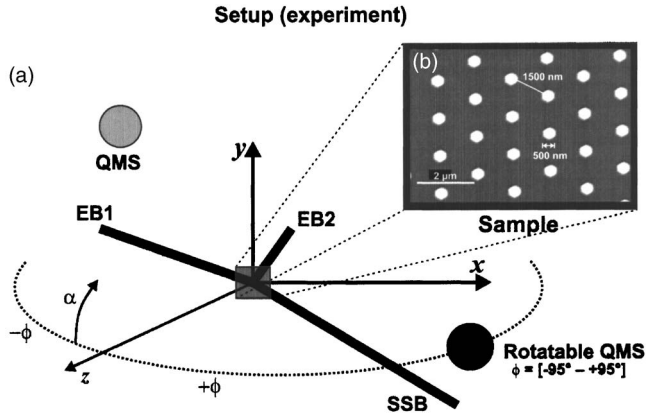

FIG. 1. (a) Experimental setup consisting of three molecular beams (EB1, EB2, and SSB), one angular-integrated mass spectrometer (QMS), and one angular-resolved mass spectrometer (rotatable QMS) and (b) SEM picture of the Pd/SiO_2 sample prepared by EBL.

Finally, the cleanliness of the Pd particles was checked by means of CO titration by molecular-beam techniques. For details on the experimental procedure we refer to previous publications.[9,17,21]

The morphology of the supported model catalyst was investigated by scanning electron microscopy) (SEM) and atomic force microscopy (AFM) prior to the experiments (at Chalmers University) and by SEM after the experiments (at the Fritz-Haber-Institute) in order to verify that no major morphological changes occurred. A SEM image is displayed in the inset of Fig. 1, which was taken after the experiments described in this work. Briefly, the sample fabricated by EBL consists of 450-nm high Pd towers with 500-nm diameter. The particles are arranged on a hexagonal array with a 1500-nm particle–particle separation (center to center). The lithographically structured area covered ~ 1 cm^2. The effective Pd area was estimated to be in the range of 8% of the geometric area.

B. Molecular-beam experiments

The experiments were performed in the UHV molecular-beam apparatus at the Fritz-Haber-Institute, already described in Ref. 23 and represented in Fig. 1. Briefly, the molecular beams of CO and O_2 were generated by two effusive beam (EB) sources and one supersonic beam (SSB) source. The beams are modulated by means of remote-controlled shutters and remote-controlled electropneumatic valves in the case of the EB sources and a remote-controlled pulsed nozzle for the SSB source.

The global reaction rates are measured with a non-line-of-sight quadrupole mass spectrometer (QMS) (Extrel). In these experiments, the incidence angles were $\phi=-25°$ and $\alpha=35°$ for the O_2 beam (99.9995%, Linde AG) and $\phi=+20°$ and $\alpha=35°$ for the CO (Linde, 99.997%, further purified by a filter Waferpure MiniXL WPMV200CO, Mykrolis GmbH) beam. The beam fluxes of CO(F_{CO}) and O_2(F_{O_2}) were chosen such that with both beams switched on the sum of the effective partial pressures $p_{eff}=p_{eff,O2}+p_{eff,CO}$ at the sample position, with $p_{eff,i}=F_{eff,i}(2p_i m_i kT)^{0.5}$ (m_i is the molecular mass of species i and T the gas tempera-

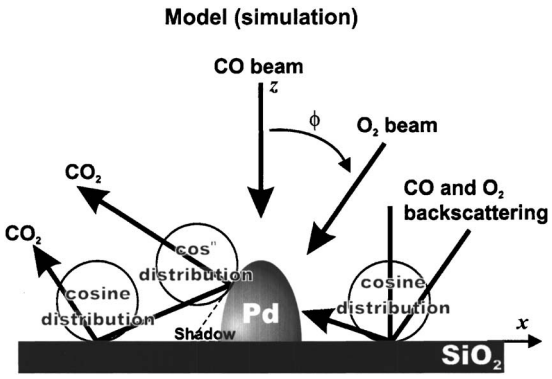

FIG. 2. Model for the simulation. The incident fluxes consist of two beams (CO and O_2) with different orientations. The Pd particle is represented as a half prolate spheroid sitting on a large disk (support). Backscattering of the product and reactants is included. The shadow of the Pd particle on the support is included in the model as well.

ture) was kept constant at 10^{-4} Pa. However, the fraction of CO in the total flux $x_{CO}=F_{CO}/(F_{O2}+F_{CO})$ was varied systematically maintaining the same p_{eff}. For the transient experiments, either the O_2 beam or the CO beam was operated in a continuous mode and the complementary beam was modulated. This procedure ensures that the steady state is approached from an oxygen precovered or CO precovered surface, respectively. A more detailed description of the experimental procedure can be found in Ref. 24.

The local reaction rates are measured by a differentially pumped and rotatable line-of-sight QMS (Hiden Analytical). The incidence angles were $\phi=60°$ and $\alpha=0°$ for the O_2 beam (SSB, 99.9995%, Linde AG) and $\phi=0°$ and $\alpha=35°$ for the CO beam (a minimum of 99% ^{13}CO, Isotec Inc., marked ^{13}CO was used in order to reduce the background level). The experiments were performed at a constant $F_{O2}=5.6\times10^{14}$ cm^{-2} s^{-1} and variable CO flux. Values for the fraction of CO in the total flux between approximately $x_{CO}=0.3$ and $x_{CO}=0.7$ were chosen. The resulting total gas fluxes were equivalent to pressures in the range of 10^{-4}–10^{-3} Pa. This experimental setup ensures that one side of the particles is completely shaded from a direct O_2 flux. For more details on the experimental procedures we refer to previous publications.[17,21] Finally, it should be noted that tests of the long-term stability of the catalyst showed no indications for CO dissociation and carbon accumulation.

C. Reaction diffusion model

In order to model the kinetics of CO oxidation on the EBL-supported model catalysts, we have recently developed a detailed RD model (see Fig. 2), which is briefly summarized in the following. For a more detailed description we refer to a previous publication.[21] The model is based on a simple mean-field (MF) description, previously used to describe CO oxidation kinetics on a homogeneous Pd surface as a function of reactant fluxes and surface temperature.[25] For the present model catalyst, the Pd surface is represented by a half prolate spheroid of appropriate diameter and height (polar radius $c=450$ nm, equatorial radius $a=250$ nm), placed on an extended disk representing the support (radius ~25 μm). Adsorption (i), surface reaction (ii), diffusion (iii), and desorption (iv) are treated for the combined particle-support system (some kinetic parameters of the previous model were adjusted to quantitatively reproduce the global kinetics on the EBL sample, for details see Ref. 21):

(i) In a first step, the reactant fluxes (F_{CO},F_{O2}) are calculated impinging on each surface element of the particle and of the support. F_{CO} is incident from $\phi=0°$, leading to a symmetric flux distribution. F_{O2} is tilted with respect to the surface normal ($\theta=0°$, $\phi=60°$). The latter results in the shading of parts of the particle on the side opposite to the O_2 beam. In addition to the direct flux, molecules can impinge on the support on which they may be either intermediately trapped and then desorb, or they can be directly backscattered into the vacuum (and in some cases hit a Pd particle after the scattering event). Both effects lead to an additional reactant flux to the metal particles and are taken into account in the model. The backscattering contribution is modeled assuming a cosine distribution from the support for both CO and O_2, and for both scattering and desorption. This assumption is justified by the fact that both trapping diffusion and direct scattering channels on the atomically rough support are expected to be rather diffuse (see Ref. 21 for details). CO adsorption on the metal occurs with a sticking coefficient S_{CO}, modeled by a Langmuir molecular adsorption term with a weak dependence of S_{CO} on Θ_O. O_2 adsorbs dissociatively with a sticking coefficient S_{O2} modeled by a Langmuir dissociative adsorption term [initial sticking coefficients $S^O_{CO}=0.7$ and $S^O_{O2}=1–7.4\times10^{-4}\,T$ K (compare Ref. 26); the latter includes a dependence on the surface temperature; other parameters are as in Ref. 21].

(ii) The Langmuir–Hinshelwood (LH) reaction event between the adsorbed species is described by a rate constant k_{LH} with an Arrhenius temperature dependence (activation energy $E_{LH}=53$ kJ mol^{-1}; preexponential factor $A_{LH}=5\times10^7$ s^{-1}, see Ref. 21 for details).

(iii) The diffusion equation is solved using the finite element method assuming that there is no flux across the particle-support boundary. This simplification can be justified by the weak interaction of the reactants with the support, leading to small capture zones in comparison with the size of the particles [see, e.g., Ref. 21, also (Refs. 2 and 4) and references therein].

An Arrhenius temperature dependence of the oxygen diffusion coefficient D_O is assumed, with $E_{diff}=55$ kJ mol^{-1} and $D_O=10^{-7}$ m^2 s^{-1}, in accordance with our previous studies[17,21] and with theoretical investigations on Pd(111).[27] For simplicity, any coverage dependence of the diffusion coefficient D_O is neglected.

As the diffusion barrier for CO on close-packed noble metal surfaces is typically small [see, e.g., Refs. 28 and 29 for CO/Pd(111)] we assume fast equilibration of the CO coverage Θ_{CO} over

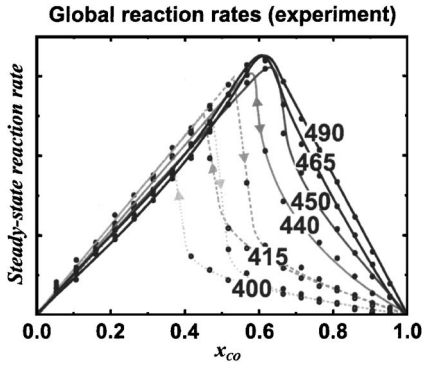

FIG. 3. Measurement of the reaction rate by the angular-integrated mass spectrometer for surface temperatures of 400, 415, 440, 450, 465, and 490 K. The hysteresis cycle is presented for $T \leqslant 440$ K, where the reaction is bistable.

the particle surface, on the time scale of the reaction. As a result Θ_{CO} is averaged over the surface of the particle to yield $\overline{\Theta_{CO}}$. Accordingly, the CO_2 formation rate on each surface element of the particle is calculated as $r_{CO_2}=\Theta_O \cdot \overline{\Theta_{CO}}$.

(iv) CO desorption from the metal is described by a rate constant k_{des} with an Arrhenius-type temperature dependence ($E_{des}=142$ kJ mol^{-1}, $A_{des}=4\times10^{14}$ s^{-1}, the reported coverage dependence of E_{des} is taken into account, see Refs. 21 and 25). O_2 desorption is neglected, which is well motivated in the temperature range considered (see, e.g., Refs. 30–33 and references therein). CO_2 interaction with the metal surface is assumed to be weak. Hence, in the model it desorbs immediately after its formation. The global CO_2 production is obtained by integration over the whole particle surface. The angular distribution of the desorbing CO_2 flux is modeled by a local $\cos^1\phi$ distribution for each Pd surface area element, in consistency with a previous analysis of the angular distribution measured on the EBL model catalyst (see Ref. 21 for details). CO_2 backscattering from the support is modeled in analogy with the backscattering of reactants. The direct and the backscattered product channels are summed and then constitute the total CO_2 angular distribution.

III. RESULTS AND DISCUSSION

A. Global reaction rates under steady-state conditions

First, we focus on the global reaction rates under steady-state conditions. A plot of the total CO_2 formation rate as a function of x_{CO} is displayed in Fig. 3. The general behavior of the rates at steady state has been investigated for various types of Pd surfaces and supported particles (see, e.g., Refs. 24, 34, and 35, see also Refs. 2 and 4, and references therein). In addition, the experiments have been subject to detailed microkinetic modeling (see, e.g., Refs. 25 and 36, see also Refs. 3 and 37, and references therein). Some general features of the experimental data displayed in Fig. 3 can be qualitatively explained on the basis of the previous models, mainly based on a homogeneous MF approach. In the following we restrict ourselves to a summary of the most important results.

In general, we can distinguish between the two reaction regimes. For small x_{CO} values (high F_{O2} and low F_{CO}) Θ_{CO} at steady state is small and Θ_O is high. This range of reaction conditions is denoted by the O-rich regime. Under these conditions, the rate determining step (RDS) of the reaction is the adsorption of CO, the rate of which is determined by the CO flux and the CO sticking coefficient. The latter is generally large and only weakly dependent on additional factors such as Θ_O and surface temperature (at least in the temperature window investigated in this work). As a result, it is found that the reaction rate is proportional to x_{CO} and nearly independent of surface temperature (see Fig. 3). At a x_{CO} value in the range of 0.35–0.7, and depending on temperature, the reaction rate reaches a maximum and then drops. The region at even higher x_{CO} is in general characterized by a large Θ_{CO} and a small Θ_O, and is denoted the CO-rich regime. Here, the most apparent difference in comparison with the O-rich region is the very low reaction rate for low surface temperatures and, hence, the strong temperature dependence of the rate at constant x_{CO}. These effects are a direct consequence of the inhibiting (poisoning) effect of preadsorbed CO on the dissociative adsorption rate of oxygen (which is the rate determining step in the limit of large x_{CO}). The temperature dependence arises from the temperature dependence of Θ_{CO} at steady state. In the limit of high temperatures (see Fig. 3), Θ_{CO} becomes small due to fast desorption and reaction and the inhibition effect on O_2 adsorption then vanishes completely. Conversely, in the limit of low sample temperatures, the inhibition effect is very pronounced and leads to strong differences in the adsorption behavior for CO and oxygen. The rapid drop of the rate of CO_2 production occurs at lower temperature; the drop is more rapid the lower the temperature is because the desorption and reaction steps that remove CO become slower and slower. The large difference in adsorption kinetics for CO and O_2, when the coverage is significant (the lower temperatures), gives rise to a so-called kinetic bistability, i.e., the existence of two stable kinetic states for a single set of reaction conditions.[37] Such bistable behavior is observed for various single-crystal surfaces and has been subject to detailed investigations (see, e.g., Refs. 37 and 38 and references therein; it is worth noting here that the occurrence of bistable kinetics is closely related to the formation of chemical waves and rate oscillations. Both phenomena have been investigated in detail, both experimentally and theoretically, see, e.g., Refs. 37–39).

In the experiment displayed in Fig. 3 the bistability window (i.e., the regime of x_{CO} values for which the bistability exists) was probed by performing two experiments at identical x_{CO}. In the first experiment, a continuous O_2 beam and a modulated CO beam are used. In the second experiment, the situation was reversed (continuous CO beam, modulated O_2 beam). As a result, the steady state is established starting from either an O-precovered or a CO-precovered surface, respectively. Within the bistability window, these two experiments lead to different steady states, characterized by large Θ_O and low Θ_{CO} (high reaction rate) and vice versa (low

reaction rate). In Fig. 3, both sets of experimental data are indicated by arrows (arrow up: CO-precovered surface; arrow down: O-precovered surface). It should be noted that a bistability window exists at surface temperatures below 440 K only. Above this critical temperature a transition to an exclusively monostable behavior occurs. This is due to the diminishing surface coverage, which in turn reduces the asymmetry in CO and O_2 adsorption kinetics; on a surface with no or nearly zero coverage there is no bistability. Finally, it should be kept in mind that a macroscopically bistable behavior can be observed on sufficiently large particles only. As has been shown recently, the macroscopic bistability is quenched on smaller catalyst particles as a result of fluctuation-induced kinetic transitions (Ref. 9, compare Refs. 8, 12, 13, and 40).

In a previous work we have performed simulations of the steady-state rate data based on a simple homogeneous MF model.[21] The experimental results were well reproduced by these simulations. However, several questions remained open with respect to the details of the kinetics. Here, one central issue concerns the pronounced local variation of reactant fluxes over the particle surface. We may ask to what extent the local variations of reactant fluxes and the resulting gradients in coverage on the particle surface play a role for the global and local reaction rates under steady-state and transient conditions as well as for the bistability behavior. Since large variations in local rates and coverages have been seen on a single particle, in simulations even with homogenous fluxes,[22] we expect significant effects.

This problem is illustrated in Fig. 4, based on the RD model (see Sec. II C). We analyze the local CO and O_2 fluxes impinging on the surface as a function of the position on the particle. Figure 4(a) shows profiles of the local F_{CO} and the local F_{O2} as a function of the position on the x axis for a cross section through the particle containing the xz plane. The reactant flux consists of two contributions: the direct flux from the beam and the flux resulting from backscattering from the support. The direct flux shows a maximum for the surface regions normal to the beam and approaches zero for the surface regions, which contain the beam direction. In the case of CO, the maximum direct flux is located on the top of the particle and the minimum is at the edges. The backscattered flux is symmetric as well and approaches a maximum at the edges, where it reaches 50% of the maximum direct flux. In contrast its contribution is zero on top of the particle. The O_2 beam is tilted from the surface normal and both contributions are asymmetric at the surface of the particle. Large direct and backscattered fluxes are present on the particle side facing the beam. On the opposite site, both direct and backscattered fluxes are low, the latter being attenuated as a result of shadowing of the particle on the support.

The strong variations of the local reactant fluxes have important consequences for the local reaction conditions on the particle surface. In Fig. 4(b) the local value $x_{CO,local}(\mathbf{r})$ is plotted as a function of the position on the particle $\mathbf{r}$ and x_{CO} in the incident beams. For $x_{CO}=0.45$, for example, the local values span a broad range between 0.3 on the side of the particle surface facing the O_2 beam and 0.8 on the shaded side. This means that, excluding CO and O diffusion, the

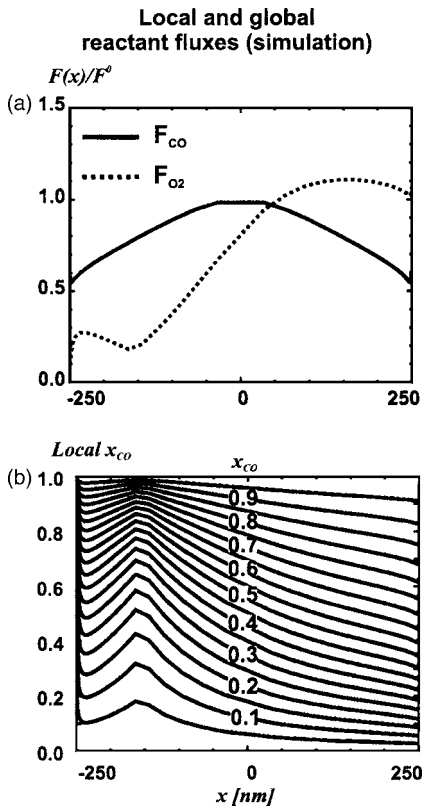

FIG. 4. (a) Total (i.e., direct flux+backscattering) O_2 and CO fluxes at the surface of the Pd particle. The profiles shown are taken along the O_2 beam direction ($\Theta_{O_2}=60°$ and $\Theta_{CO}=0°$). (b) Calculated profiles of the local x_{CO} for different global x_{CO} along the O_2 beam direction.

local reaction conditions at the particle surface typically vary between O rich and CO rich as a function of position on the particle surface. Therefore, the local reactant coverages established under transient and steady-state conditions are expected to be critically dependent on CO and O diffusion lengths on the time scale of their residence on the surface.

Figure 5(a) displays a simulation of the steady-state rates, as derived from the RD model. Based on a previous study, we use an activation energy for O diffusion of 55 kJ/mol (Ref. 21) and assume fast CO diffusion on the time scale of CO residence. The results of the RD model quantitatively reproduce the experimental data (cf. Fig. 3) both as a function of x_{CO} and of surface temperature (from 400 to 490 K). All deviation in x_{CO} are within the experimental error limits. Similarly, this holds for the width and temperature region of the bistability region, which is also well described.

In a second step, we compare the RD model to the simple homogeneous MF approach used previously, which does not take surface diffusion into account (Ref. 25, see also Ref. 9). In order to obtain comparable data, we calculate the average CO flux $\langle F_{CO}\rangle$ and O_2 flux $\langle F_{O2}\rangle$ onto the particle surface. We then use these averaged fluxes in the RD model; diffusion is suppressed by the averaging but the morphology of the particle is kept. In the following, we refer to this situation as the homogeneous flux (HF) model. Figure 5 shows the corresponding results.

Comparing the two models, it can be noticed that the

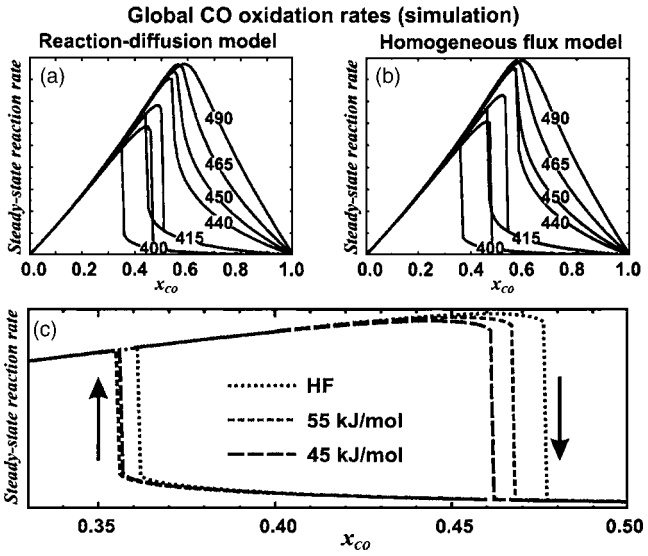

FIG. 5. Global reaction rates obtained from two different models: (a) RD model (E_{diff}=55 kJ/mol) and (b) homogeneous flux model. (c) The bistable regime is investigated for T=440 K, E_{diff}=45 and 55 kJ/mol, and the homogeneous flux model (HF).

differences in the global rate are very small, both under CO-rich and O-rich conditions. Also, the shift of the bistability region is minor [see Fig. 5(c)]. It can be concluded that the differences between the two models are typically within the accuracy of our experiments. These results show that for the present type of model catalyst, effects arising from the inhomogeneous distribution of the reactants will not lead to significant changes of the global rate. Therefore, effects related to local variations of the reaction rates cannot be identified via simple angle-integrated rate measurements. However, it has been shown recently that strong local variations of Θ_{O} are established under CO-rich conditions.[17]

Qualitatively, the similarity of the global rates can be understood as follows: (1) Under O-rich conditions the diffusion of both CO and O is fast on the time scale of the reaction. Hence we expect equilibration of the surface coverages and, as a result, the RD and the HF model should yield very similar results. (2) Under CO-rich conditions, on the other hand, there is no equilibration of Θ_{O} over the particle surface. The simulations, however, show that the differences in the rate predicted by the two models are small. This can be understood by the fact that under CO-rich conditions, the RDS is the dissociative adsorption of O_2. The reaction probability for this step is primarily controlled by Θ_{CO}, which depends on CO adsorption–desorption equilibrium. Concerning Θ_{CO}, it should be noted that there is fast equilibration over the particle surface and that the sticking coefficient for CO is only weakly affected by the O precoverage (i.e., no oxygen poisoning). It follows that there is only a weak effect of the distribution of Θ_{O} on Θ_{CO}. Moreover, CO diffusion over the particle leads to synchronization of the switching behavior over the whole particle. The latter is indicated by the well-defined transition between the two regimes upon leaving the bistability window.

B. Local reaction rates under steady-state conditions

In a second step, we investigate the local reaction rates on the Pd particles as a function of x_{CO}. For this purpose the dependence of the reaction rate on x_{CO} is measured using angle-resolved mass spectrometry at detection angles of $\phi=+70°$ (i.e., on the particle side facing the O_2 beam) and $\phi=-70°$ [i.e., on the particle side opposite to the O_2 beam, see Fig. 6(a)].

The reaction rates (normalized to their maximum value) are displayed in Fig. 6(b). For both detection angles, the maximum rate indicates the transition between O-rich and CO-rich regimes. The position of the maximum rate is slightly shifted for the two detection angles. It occurs at $x_{\mathrm{CO}}=0.53\pm0.02$ for $\phi=-70°$ and $x_{\mathrm{CO}}=0.58\pm0.02$ for $\phi=+70°$.

In view of the drastic variations of the local fraction of CO in the impinging flux $x_{\mathrm{CO,local}}(\mathbf{r})$ as a function of the position on the particle surface (see Sec. III A) the changes in the transition point between the O-rich and the CO-rich regimes are rather small. This experimental observation indicates that, as discussed in Sec. III A, the transition between the reaction regimes occurs in a largely synchronized fashion over the entire particle surface. This behavior is in agreement with the global steady-state experiments, which showed a well-defined switching behavior between the regimes as a function of x_{CO} (see Sec. III A).

In order to further explore the switching behavior between the reaction regimes, we have performed simulations of the local reaction rates as a function of x_{CO}, both below

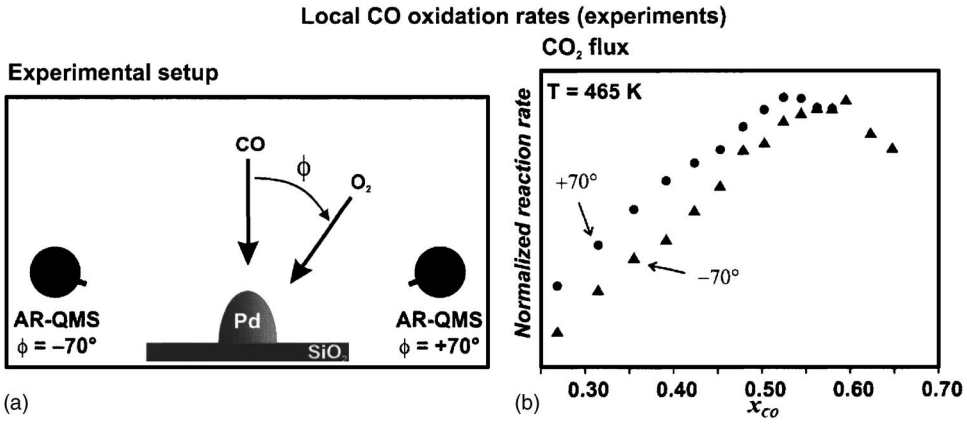

FIG. 6. (a) Scheme of the experimental setup, the AR QMS is positioned at $\phi=+70°$ and $\phi=-70°$ and (b) the CO_2 production is measured at these two positions, at T=465 K.

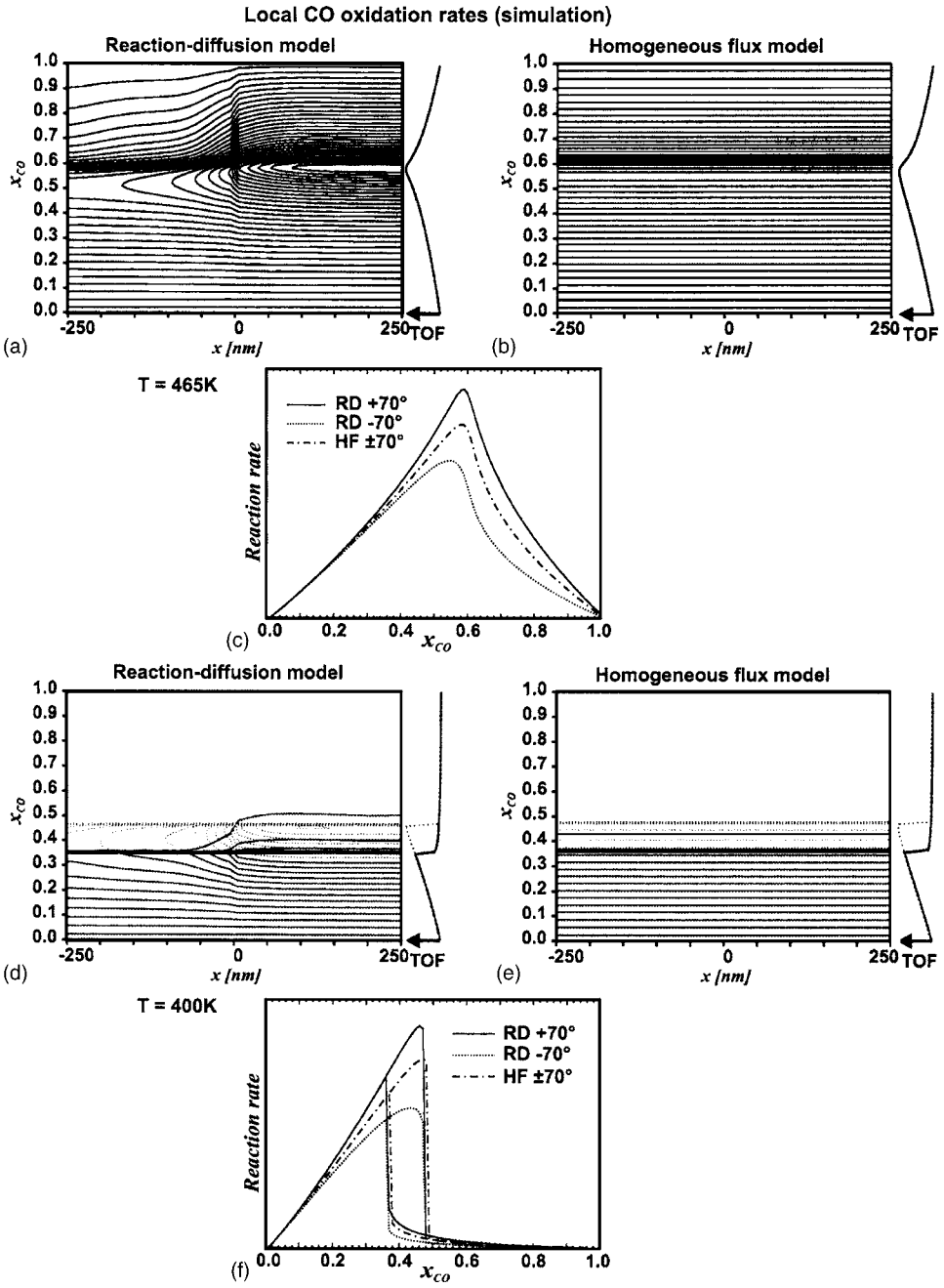

FIG. 7. Simulation of the experiment in Fig. 6, using the RD model [(a) and (c) $T=465$ K, $E_{\mathrm{diff}}=55$ kJ/mol; (d) and (f) $T=400$ K, $E_{\mathrm{diff}}=55$ kJ/mol] and HF model [(b) and (c) $T=465$ K; (e) and (f) $T=400$ K]. The local reaction rate (marked turn-over frequency, TOF) along the O_2 beam direction is plotted on contour plots for $0.0 \leqslant x_{\mathrm{CO}} \leqslant 1.0$ [(a)–(e)]. The global (integrated) reaction rate is also presented for both models [(c) and (f)].

the critical temperature, i.e., in the presence of the bistability window, and above the critical temperature, i.e., in absence of the kinetic bistability.

We first focus on the behavior above the critical temperature. Figures 7(a) and 7(b) show contour plots of the reaction rates as a function of position and x_{CO}. Again, we compare the results of the RD model with the HF approach.

For the HF model [Fig. 7(b)] the reaction rates are independent of the position on the particle. They increase linearly with increasing x_{CO}. Then they drop rapidly upon transition to the CO-rich regime for $x_{\mathrm{CO}}>0.6$. For the RD model, there is nearly no gradient in the local reaction rates in the limit of small x_{CO}. For $x_{\mathrm{CO}}>0.3$, however, the gradient in the rates become successively larger. It should be noted that in the vicinity of the transition point, the rates on the shaded side of the particle are only slightly dependent on x_{CO}, whereas they increase strongly on the side facing the O_2 beam. This effect is related to a pronounced change in Θ_{O} in this region, leading to a strong decrease in O diffusion length. As a result, the maximum reaction rates appear at slightly different x_{CO} values on the two sides of the particle. This observation is in full agreement with the experimental results discussed above. In order to compare directly with the experimental data in Fig. 6, the effective reactant flux for the two detection angles was calculated [Fig. 7(c), see model in Sec. II C]. It is found that the shift of the maximum rate as a function of the detection angle is very well reproduced by the RD model.

In spite of the shift of the maximum rate on different parts of the particle, the actual transition between the two regimes, indicated by the steep drop in the CO_2 production rate, occurs at $x_{\mathrm{CO}}=0.6$ in a nearly synchronous fashion on both sides of the particle. This observation supports the pre-

vious suggestion that the transition between the two reactive states does not occur independently on different parts of the particle, but is mainly triggered and synchronized by Θ_{CO} and fast CO diffusion over the particle, which couple the reaction rates over the complete particle surface.

In Figs. 7(d)–7(f) corresponding data are displayed for a surface temperature below the critical temperature. Briefly, the behavior upon switching between the regimes is very similar to the situation at higher temperature. Close to the transition point, the gradient of the reaction rate increases rapidly as a result of the decreasing O residence time. This gives rise to a maximum in the rate appearing at slightly different x_{CO}. The actual transition to the CO-rich regime, however, occurs at a well-defined x_{CO} in a synchronous fashion over the complete particle surface. The same is true for transition from the CO-rich to the O-rich regime.

C. Global reaction rates under transient conditions

Finally, we investigate the kinetics under transient conditions. Figure 8 displays representative experimental results for the transient reaction rates. The data were obtained using a modulated O_2 beam and a continuous CO beam [Fig. 8(a); this means that the steady state with both beams operating is approached starting from a CO-precovered surface] and using a modulated CO beam and a continuous O_2 beam [Fig. 8(b); i.e., the steady state is approached from an O-precovered surface].

For the CO-precovered case we find two characteristic types of transient behavior. For low x_{CO}, we observe a steep maximum after admission of the O_2 beam before the reaction rate reaches the steady state. The CO_2 formation rate initially increases in a slow and continuous fashion upon admission of the O_2 beam. The time after which a transient rate maximum is observed increases with increasing x_{CO}. At the same time the height of the transient maximum decreases. Upon switching to the CO-rich regime, there is a steplike decrease in the rate. Simultaneously, the transient maximum in the CO_2 production rate disappears and the steady state is reached in a monotonous fashion. Under CO-rich conditions, the steady-state CO_2 production rate decreases, as well as the time scale on which it is reached.

For the O-precovered surface, a completely different transient behavior is found. Both in the O-rich and in the CO-rich reaction regimes, we find an instantaneous increase in the reaction rate upon admission of the CO beam on the time scale of the experiment (typically in the order of 50 ms). This sudden increase is followed by a slower transient region. Under O-rich conditions ($x_{CO}<0.50$), the reaction rate approaches the steady-state level in a monotonous fashion. In contrast, a transient maximum develops under CO-rich conditions, before a steady-state rate level lower than under O-rich conditions is reached. A second maximum appears after termination of the beam, which is not discussed here (see Refs. 24, 25, and 35 for details). A special type of transient behavior is observed in the vicinity of the bistability region, i.e., immediately after the transition from one regime to the other. The corresponding transients are displayed in Fig. 8(c). It is observed that the time scale diverges, on

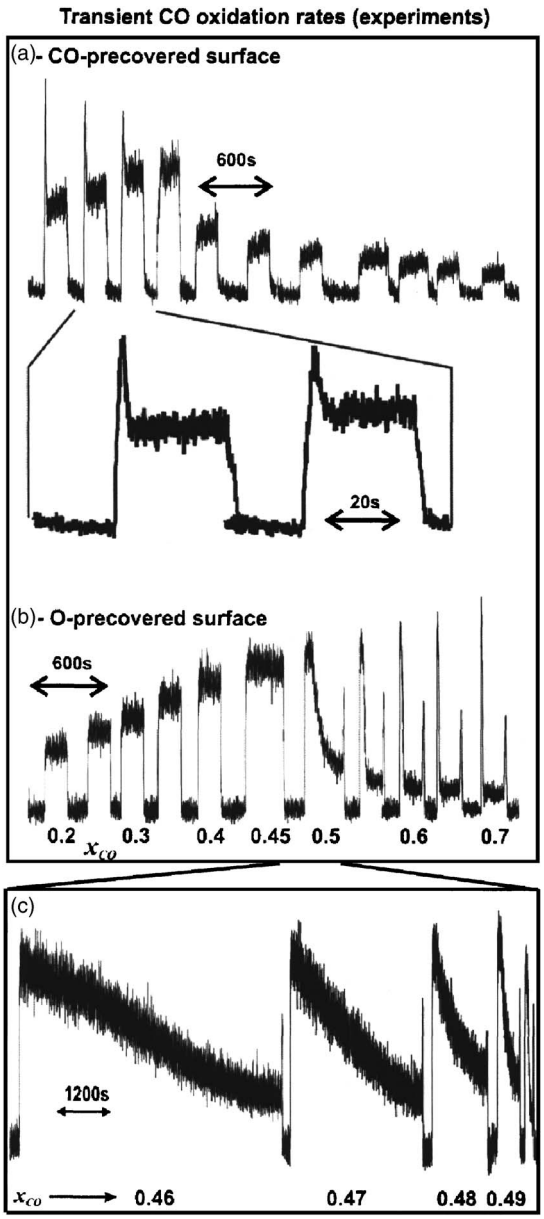

FIG. 8. CO_2 transient measured at $T=400$ K on (a) a CO-precovered surface and [(b) and (c)] an O-precovered surface.

which the steady-state level is reached. Experimentally, this means that, for example, with the O_2 beam operating in a continuous more, upon adding the CO beam it may take a very long time before a constant reaction rate is reached. Very close to the bistability window ($x_{CO}<0.49$), transient times in the order of 10^3–10^4 s are observed experimentally.

In the following we discuss the global transient behavior on the basis of microkinetic simulations based on the RD and HF models. The corresponding results are displayed in Figs. 9 and 10. In Fig. 9, two sets of data are displayed as a function of x_{CO}, corresponding to a reaction temperature below the critical temperature [Fig. 9(a), $T=400$ K, with bistability] and above the critical temperature [Fig. 9(b), $T=465$ K, without bistability]. The two types of transients for the CO-precovered surface (solid lines) and for the O-precovered surface (dashed lines) are directly compared. In Fig. 10(a) (CO-precovered surface, modulated O_2 beam)

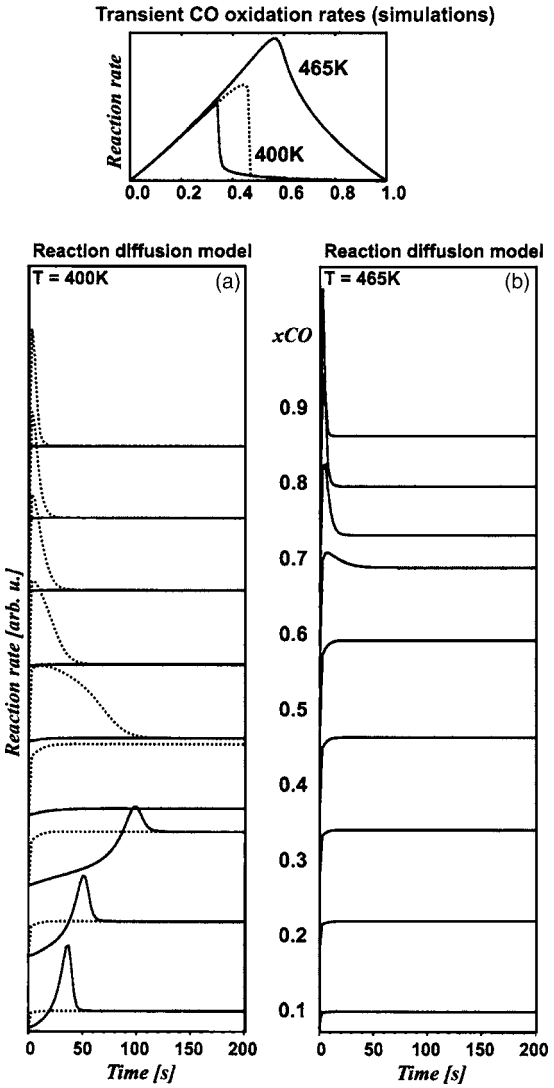

FIG. 9. Transient CO_2 production calculated for $T=400$ K and $T=465$ K by means of the RD model ($E_{diff}=55$ kJ/mol). Continuous CO beam and modulated O_2 beam (CO-precovered surface), solid line; continuous O_2 beam and modulated CO beam (O-precovered surface), dashed line.

and Fig. 10(b) (O-precovered surface, modulated CO beam), we have selected five representative regimes for a reaction temperature below the critical temperature:

(i) in the O-rich regime,
(ii) in the O-rich regime close to the bistability window,
(iii) in the bistable regime,
(iv) in the CO-rich regime close to the bistability window, and
(v) in the CO-rich regime.

In addition to the reaction rates, the average Θ_O and Θ_{CO} on the particle (RD and HF models) and the profiles of Θ_O (RD model; along a cross section through the particle containing the *yz* plane) are displayed as a function of time. In the following, we discuss these five types of typical transient behavior in detail (due to the similarity between the RD and HF models, the results for the HF model are shown for the CO-precovered case only):

(i) Under O-rich conditions [Fig. 9(a); $0 \leqslant x_{CO} \leqslant 0.3$; Fig. 10], the reaction rate shows a transient maximum for the CO-precovered case only. From the coverages plotted in Fig. 10, we see that this maximum occurs for conditions under which Θ_{CO} decreases rapidly, whereas at the same time Θ_O increases. The product of both quantities, which determines the reaction rate in the microkinetic models, goes through a maximum. After this maximum, the decrease in Θ_{CO} dominates over the increase in Θ_O leading to a decreasing global rate. Under O-precovered conditions, Θ_O remains high and Θ_{CO} remains low in the transient region, giving rise to a monotonous transient behavior. One thing to be noted is that the initial reaction rate upon switching on the O_2 beam is low for the CO-precovered case and increases slowly on a time scale which depends on x_{CO}. This behavior is in sharp contrast with the transient behavior under CO-rich conditions (see below). The low rate observed initially is the result of the low probability for dissociative adsorption of O_2 on the CO precovered surface (dissociative adsorption of O_2 is the RDS under these conditions). The latter is the consequence of the strongly inhibiting effect of CO on the O_2 chemisorption.

Comparing the RD and HF flux models, it is noteworthy that the differences in the transient kinetics and in the average coverages are minor. This similarity is a direct consequence of the fast diffusion of both CO and O on the time scale of surface residence at steady state under O-rich conditions. As a result, there is a nearly complete equilibration of adsorbed oxygen and the gradient of Θ_O vanishes. However, in the transient region starting from a CO-precovered situation, the initial gradient of Θ_O is large, indicating a drastically reduced residence time and diffusion length. The gradient decreases as Θ_O increases. Still the behaviors of the global transient and of the average coverages develop similarly for both RD and HF models. This indicates that fast diffusion of CO results in a coupling of the transient response over the complete particle surface. This effect is similar to the behavior under the steady state discussed in the previous sections.

(ii) A special type of transient behavior is observed in the O-rich region in close proximity to the bistability region (Fig. 10). Here it is found that for the CO-precovered case the transient time required to establish the steady state becomes extremely long. In close vicinity of the bistability window [see Figs. 10(a) and 10(b)], the system remains for a limited time in a CO-rich regime. This state is unstable, however, and the system slowly drifts towards O-rich conditions. This drift involves a slow increase of Θ_O over the particle until a rapid transition to the O-rich state occurs. For the O-precovered case, Θ_O remains high and no transient maximum occurs [experimentally, this

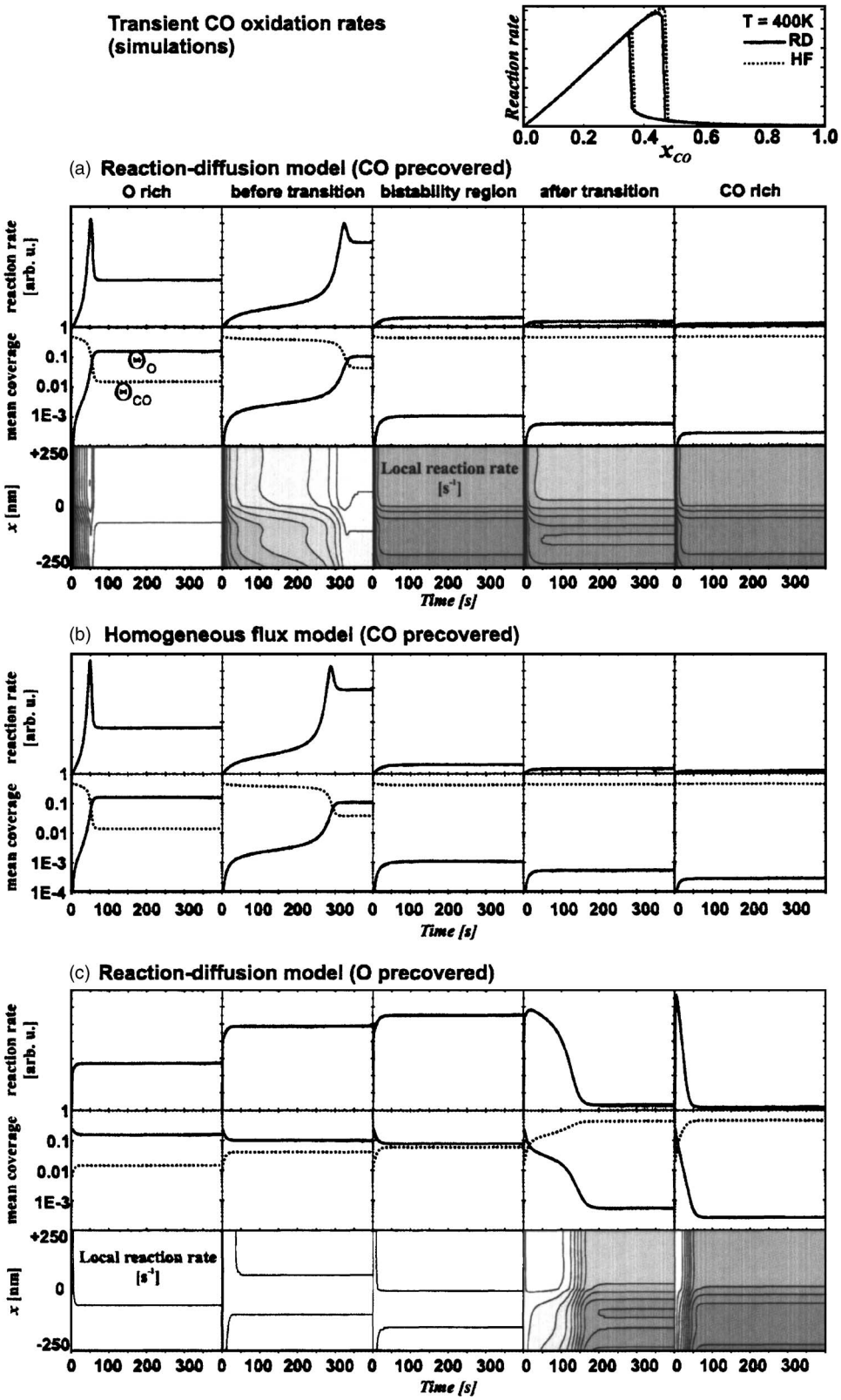

FIG. 10. Time evolution at $T=400$ K of the CO_2 production (first row); mean coverages (second row) and local reaction rates [third row for (a) and (c)] for $x_{CO}=0.2$ (first column), 2% before the bifurcation [second column, $x_{CO}=0.35$ (RD); $x_{CO}=0.353$ (HF)] in the bistable region, $x_{CO}=0.4$ (third column); 2% after the bifurcation [fourth column $x_{CO}=0.477$ (RD); $x_{CO}=0.487$ (HF)], and $x_{CO}=0.6$ (fifth column). [(a) and (c)] The RD model is used ($E_{diff}=55$ kJ/mol) for the O-precovered and the CO-precovered situation. (b) HF model (only the case of CO precoverage is shown because of the close similarity of the results obtained via both models). The local reaction rates for the RD model are shown on grayscales. The reaction rate r is plotted on a logarithmic scale. Again, the rate is shown for a cross section of the particle containing the xz-plane (see Fig. 1 for the geometry of the experiment).

behavior is seen around $x_{CO}=0.35$ in Fig. 8, but more clearly this slow type of transient behavior is observed on the CO-rich side of the bistability window; see case (iv), discussed below].

Again the differences in the global rate predicted by the RD and the HF models are minor. It should be noted that the transient behavior described here should be distinguished from the slow transient behavior observed in previous work for smaller particles.[9] In the latter case it was found that macroscopic bistabilities were quenched for an ensemble of particles as a result of spontaneous transitions between the kinetic

regimes due to large coverage fluctuations on small particles.

(iii) Within the bistability window [Fig. 9(a); $x_{CO}=0.4$; Fig. 10], both the RD and HF models predict two kinetic states, which are perfectly stable as a function of time. The transient behavior is monotonous for both states. This is a consequence of the absence of drastic changes in coverage in the transition region.

(iv) For the CO-precovered case the reaction rate develops monotonously in the CO-rich regime (Fig. 10) close to the bistability region. For the O-precovered case, on the other hand, the behavior is comparable to the O-rich regime with CO precoverage in that the transient time diverges. The system now remains some time at high Θ_O. The O-rich state is unstable, however, and slowly drifts toward lower Θ_O and higher Θ_{CO} up to a point where a sudden switch to the CO-rich state occurs. It should be noted that this characteristic transient behavior is observed experimentally as well [see Fig. 8(c)]. Again a synchronized switching of the complete particle occurs for the RD model as a result of coupling via CO diffusion, resulting in a similar global transient response for the HF and the RD model.

(v) In the CO-rich regime [Fig. 9(a); $0.5 \leqslant x_{CO} \leqslant 1$; Fig. 10] the transient response is the inverse of the O-rich regime in that the transient maximum occurs for O precoverage, and not for CO precoverage. Again the maximum CO_2 production appears under conditions of rapidly decreasing Θ_O and simultaneous rapidly increasing Θ_{CO} at an optimal coverage ratio. Similarly to the O-rich regime, the transient response becomes increasingly fast with increasing distance from the bistability region. An important difference between the transient behavior for CO precoverage and O precoverage is visible in the initial response upon impingement of the O_2 or CO beam, respectively. This is particularly evident under conditions at which there is a transient rate maximum (CO precoverage for O-rich conditions and O precoverage for CO-rich conditions). For the O-precovered situation, there is an immediate increase in the rate upon impingement of the CO beam. Under conditions of CO precoverage, on the other hand, the rate increases slowly after admission of O_2. The immediate increase in the rate is a result of the high sticking coefficient of CO on the O-precovered surface. A weakly bound precursor state, with a low steady-state coverage, starts the adsorption of CO. Chemisorption occurs from this precursor state with high probability and weak dependence on the CO and O precoverages. Chemisorption is followed by immediate oxidation to CO_2 with a high Θ_O (CO adsorption being the RDS under these conditions) leading to an immediate response in the CO_2 signal (see also discussion in Refs. 24 and 41). In contrast, the dissociative adsorption of O_2 is strongly inhibited on a CO-precovered surface, leading to a very low initial reaction rate until a part of the CO layer is removed. Comparing the RD and HF models, it is again observed that the differences between both approaches are minor with respect to the predicted global rates. As discussed before, the similarities between both models are attributed to the coupling of the coverages and rates over the particle surface via fast CO diffusion.

A final remark concerns the comparison between the experimental results (Fig. 8) and the simulations (Figs. 9 and 10). It can be concluded that all characteristic features of the transient experiments are well reproduced by the simulations. This holds not only for the general type of the transient behavior but also for the details discussed above. In general, it can be concluded that for the present type of model catalyst the global transient kinetics are well described by both the RD and HF models, whereas an accurate description of the local reaction rates on the particle surface requires an explicit description of diffusion processes by the RD model.

It should be pointed out, however, that the situation might be different in case of model catalysts based on well-oriented and faceted nanoparticles, as opposed to the polycrystalline particles used here. The presence of differently oriented facets may give rise to changes in the global rate as a function of the distribution of the reactant fluxes onto the particle. The situation may be further complicated by edges at facet boundaries (see, e.g., Ref. 3). Future experimental work on such structurally well-defined supported nanocrystallites, in combination with the simulation approaches presented in this paper, may help to provide detailed insights into the reaction-diffusion coupling on supported catalysts and into the related kinetic phenomena.

IV. CONCLUSIONS

We have investigated the local and global kinetics of CO oxidation on a supported $Pd/SiO_2/Si(100)$ model catalyst, consisting of a well-defined array of large Pd particles (500-nm diameter, 450-nm height) prepared by means of electron-beam lithography. Employing molecular-beam methods, angle-resolved and angle-integrated mass spectrometries, the local and global reaction kinetics were probed under steady-state and transient conditions. Both, monostable and bistable regimes were investigated. The experimental results were analyzed in terms of two types of microkinetic models. A simple microkinetic mean-field model assuming homogeneous surface and homogeneous reactant fluxes (HF) and a detailed reaction-diffusion model (RD). Both models take into account the morphology of the catalyst, the geometry of the molecular-beam experiment as well as scattering form of the support.

(i) *Global steady-state kinetics*. In spite of the strong local variations of the reactant fluxes over the particle surface and the limited oxygen mobility, it is found that the global reaction rates show temperature and flux dependences similar to single-crystal studies. Also in analogy to single crystals, a well-defined bistability window is observed. The results are quantitatively reproduced by both RD and HF models. The existence of bistability is

attributed to the coupling of the surface coverages and reaction rates over the complete particle surface via fast CO diffusion. As a result, switching between the regimes occurs over the full surface of the particle at a well-defined ratio of reactant fluxes.

(ii) *Local steady-state kinetics*. Local reaction rate measurements via angle-resolved mass spectrometry show a nearly synchronous switching behavior between the CO- and O-rich regimes over the full particle surface. On the basis of microkinetic simulations it is shown that the transition between the kinetic regimes is largely driven by the surface mobility of CO. In spite of the synchronous kinetic phase transition, pronounced gradients of oxygen coverage and reaction rate persist over the particle surface under CO-rich reaction conditions. This effect, which is the result of the limited O diffusion length, can only be quantitatively described only by the RD model.

(iii) *Global transient kinetics*. Different types of transient behavior are observed in the various kinetic regimes, i.e., under CO-rich conditions, in the bistable regime and under O-rich conditions, depending on the initial conditions of the surface (either O or CO precoverage). All characteristic types of global transient behavior are well described by the HF model, whereas a description of the local distribution of rates over the particle surface requires a RD model.

These results demonstrate that the global CO oxidation kinetics of a model catalyst, when its surface is exposed to reactant fluxes showing strong local variations, are similar to the kinetics observed on single-crystal surfaces. This prediction holds even for very large particle sizes as a result of fast surface diffusion of CO. With respect to microkinetic simulations, the behavior is well described by a homogeneous surface model (mean field), under both transient and steady-state conditions. In spite of the single-crystal-like global kinetic behavior there may exist pronounced gradients in the coverage of one reactant and the local reaction rates. The analysis of these effects, which contain information on the surface mobility of the individual reactants, requires microkinetic simulations based on a detailed reaction-diffusion model.

ACKNOWLEDGMENTS

We acknowledge the support of the Deutsche Forschungsgemeinschaft, the Fonds der Chemischen Industrie, and of the Competence Center for Catalysis at Chalmers, supported by the Swedish Energy Administration, Chalmers, and its member companies: AB Volvo, Johnson Matthey CSD, Saab Automobile Powertrain AB, Persorp AB, MTC AB, Eka Chemicals, and the Swedish Space Administration. One of the authors (M.L.) thanks C. Beta (FHI Berlin) for helpful preliminary discussions. We thank G. Weinberg (FHI Berlin) for the SEM images of the lithographically prepared model catalyst.

[1] *Handbook of Heterogeneous Catalysis*, edited by G. Ertl, H. Knoezinger, and J. Weitkamp (VCH, Weinheim, 1997).
[2] C. R. Henry, Surf. Sci. Rep. **31**, 231 (1998).
[3] V. P. Zhdanov and B. Kasemo, Surf. Sci. Rep. **39**, 25 (2000).
[4] J. Libuda and H.-J. Freund, Surf. Sci. Rep., **57**, 157 (2005).
[5] V. P. Zhdanov and B. Kasemo, Surf. Sci. **405**, 27 (1998).
[6] V. P. Zhdanov and B. Kasemo, Phys. Rev. B **55**, 4105 (1997).
[7] V. P. Zhdanov and B. Kasemo, J. Catal. **170**, 377 (1997).
[8] V. P. Zhdanov and B. Kasemo, Surf. Sci. **496**, 251 (2002).
[9] V. Johánek, M. Laurin, A. W. Grant, B. Kasemo, C. R. Henry, and J. Libuda, Science **304**, 5677 (2004).
[10] V. P. Zhdanov, Surf. Sci. Rep. **45**, 233 (2002).
[11] K. A. Fichthorn, E. Gulari, and R. M. Ziff, Phys. Rev. Lett. **63**, 1527 (1989).
[12] Y. Suchorski, J. Beben, E. W. James, J. Evans, and R. Imbihl, Phys. Rev. Lett. **82**, 1907 (1999).
[13] Y. Suchorski, J. Beben, R. Imbihl. E. W. James, D.-J. Liu, and J. W. Evans, Phys. Rev. B **63**, 165417 (2001).
[14] C. R. Henry, in *The Chemical Physics of Solid Surfaces, Surface Dynamics*, edited by D. P. Woodruff (Elsevier, Amsterdam, 2003), Vol. 11.
[15] J. Libuda and H.-J. Freund, J. Phys. Chem. B **106**, 4901 (2002).
[16] J. Libuda, ChemPhysChem **5**, 625 (2004).
[17] V. Johanek, M. Laurin, J. Hoffmann, S. Schauermann, A. W. Grant, B. Kasemo, J. Libuda, and H.-J. Freund, Surf. Sci. Lett. **561**, L218 (2004).
[18] K. Wong, S. Johansson, and B. Kasemo, Faraday Discuss. **105**, 237 (1996).
[19] M. X. Yang, D. H. Gracias, P. W. Jacobs, and G. A. Somorjai, Langmuir **14**, 1458 (1998).
[20] J. Hoffmann, S. Schauermann, J. Hartmann, V. P. Zhdanov, B. Kasemo, J. Libuda, and H.-J. Freund, Chem. Phys. Lett. **354**, 403 (2002).
[21] M. Laurin, V. Johanek, A. W. Grant, B. Kasemo, J. Libuda, and H.-J. Freund, J. Chem. Phys. (in press).
[22] H. Persson, P. Thormahlen, V. P. Zhdanov, and B. Kasemo, Catal. Today **53**, 273 (1999).
[23] J. Libuda, I. Meusel, J. Hartmann, and H.-J. Freund, Rev. Sci. Instrum. **71**, 4395 (2000).
[24] J. Libuda, I. Meusel, J. Hoffmann, J. Hartmann, L. Piccolo, C. R. Henry, and H.-J. Freund, J. Chem. Phys. **114**, 4669 (2001).
[25] J. Hoffmann, I. Meusel, J. Hartmann, J. Libuda, and H.-J. Freund, J. Catal. **204**, 378 (2001).
[26] T. Engel, J. Chem. Phys. **69**, 373 (1978).
[27] K. Honkala and K. Laasonen, J. Chem. Phys. **115**, 2297 (2001).
[28] E. G. Seebauer and C. E. Allen, Prog. Surf. Sci. **49**, 265 (1995).
[29] M. Snabl, O. Borusik, V. Chab, M. Ondrejcek, W. Stenzel, H. Conrad, and A. M. Bradshaw, Surf. Sci. **385**, L1016 (1997).
[30] G. Zheng and E. I. Altman, Surf. Sci. **462**, 151 (2000).
[31] G. Zheng and E. I. Altman, Surf. Sci. **504**, 253 (2002).
[32] F. P. Leisenberger, G. Koller, M. Sock, S. Surnev, M. G. Ramsey, F. P. Netzer, B. Klötzer, and K. Hayek, Surf. Sci. **445**, 380 (2000).
[33] B. Klötzer, K. Hayek, C. Konvicka, E. Lundgren, and P. Varga, Surf. Sci. **482**, 237 (2001).
[34] C. Becker and C. R. Henry, Surf. Sci. **352–354**, 457 (1996).
[35] I. Meusel, J. Hoffmann, J. Hartmann, J. Libuda, and H.-J. Freund, J. Phys. Chem. B **105**, 3567 (2001).
[36] L. Piccolo, C. Becker, and C. R. Henry, Eur. Phys. J. D **9**, 415 (1999).
[37] V. P. Zhdanov and B. Kasemo, Surf. Sci. Rep. **20**, 111 (1994).
[38] R. Imbihl and G. Ertl, Chem. Rev. (Washington, D.C.) **95**, 697 (1995).
[39] S. Jakubith, H. H. Rotermund, W. Engel, A. V. Oertzen, and G. Ertl, Phys. Rev. Lett. **65**, 3013 (1990).
[40] Y. Suchorski, J. Beben, and R. Imbihl, Surf. Sci. **454**, 331 (2000).
[41] L. Piccolo, C. Becker, and C. R. Henry, Appl. Surf. Sci. **164**, 156 (2000).